Methanol Adsorption and Dissociation on $LaMnO_3$ and Sr Doped $LaMnO_3$ (001) Surfaces

Ariana Beste

PII: S0039-6028(17)30295-9
DOI: 10.1016/j.susc.2017.06.010
Reference: SUSC 21050

To appear in: *Surface Science*

Received date: 21 April 2017
Revised date: 7 June 2017
Accepted date: 9 June 2017

Please cite this article as: Ariana Beste, Methanol Adsorption and Dissociation on $LaMnO_3$ and Sr Doped $LaMnO_3$ (001) Surfaces, *Surface Science* (2017), doi: 10.1016/j.susc.2017.06.010

Highlights

- DFT study of methanol adsorption and dissociation on MnO_2 and LaO terminated $LaMnO_3$ (001) surfaces as a function of Sr dopant enrichment
- Electron depletion in negatively charged MnO_2 surface layer enhanced by Sr doping
- Electron accumulation in positively charged LaO surface layer reduced by Sr doping
- Dissociative methanol adsorption strongly preferred on LaO termination over MnO_2 termination in $LaMnO_3$ and moderately doped $LaMnO_3$
- For highly Sr enriched surfaces, methanol favors dissociative adsorption on MnO_2 termination over LaO termination

Methanol Adsorption and Dissociation on $LaMnO_3$ and Sr Doped $LaMnO_3$ (001) Surfaces

Ariana Beste[a,*]

[a] *Joint Institute for Computational Sciences, The University of Tennessee, Oak Ridge, TN 37831*

Abstract

Using density functional theory, we investigate methanol adsorption and dissociation on the MnO_2- and LaO-terminated $LaMnO_3$ (001) surface as a function of Sr dopant enrichment in and near the surface. In response to bulk cleavage, we find electron depletion of the negatively charged MnO_2 surface layer that is enhanced by Sr doping in the subsurface. In contrast, we observe electron accumulation in the positively charged LaO surface layer that is reduced by Sr doping in the surface layer. Methanol adsorbs dissociatively on the LaO termination of the $LaMnO_3$ (001) surface. Methanol adsorption on the LaO termination is strongly preferred over adsorption on the MnO_2 termination. While moderate doping has a small influence on methanol adsorption and dissociation, when 100% of La is replaced by Sr in the surface or subsurface, the adsorption preference of methanol is reversed. If the surface is highly dopant enriched, methanol favours dissociative adsorption on the MnO_2-terminated surface.

Keywords: perovskite, strontium dopant, LMO, LSMO, VASP, DFT,

*Corresponding author
Email address: bestea@ornl.gov (Ariana Beste)

revPBE, Bader charges

---

1. Introduction

Perovskites are a family of well defined oxide materials of composition ABO_3, where A is a large cation of similar size as the oxygen ion and B is a smaller cation filling octahedral holes created by the closed packed lattice of oxygen and A ions. The perovskite structure is very flexible and can accommodate a large number of different A and B ions leading to a great variety of materials. One example of a perovskite material is lanthanum manganite, $LaMnO_3$. It is the parent compound of several important materials ($A_{(1-x)}A'_xMnO_3$) that show colossal magnetoresistivity [1]. In addition, $LaMnO_3$ and its doped variants attracted a lot of attention due to their application as a cathode material in solid oxide fuel cells [2]. Our interest in perovskite materials stems from the possibility of tuning catalytic properties of oxides using the flexibility in composition through A and B site occupation as well as doping type and range. We probe acid/base and redox sites of mixed oxides using conversion reactions of oxygenates with the goal of designing a highly selective and efficient catalyst. Methanol has previously been used by us as a probe reaction to characterize cerium oxide catalysts [3, 4, 5]. Here, we study methanol adsorption and dissociation on $LaMnO_3$ and Sr doped $LaMnO_3$ surfaces using density functional theory (DFT).

The ideal perovskite structure ($CaTiO_3$) is cubic. The tolerance factor [6] (t) is a measure of the radii differences between A, B, and oxygen ions and ranges between 0.75 and 1.0 in stable perovskites [7]. Depending on the tolerance fctor, many perovskites assume a distorted geometry. In $LaMnO_3$ (t=0.94 [8]), La^{3+} is smaller than O^{2-} and the MnO_6 octahedra tilt to fill space. Further, the octahedra are elongated due to the Jahn-Teller effect

that allows for energy lowering when degenerate orbitals are partially occupied. The resulting structure for $LaMnO_3$ is orthorhombic and can be described within the Pnma [9] or, equivalently, within the Pbnm [10] space group. In the ground state, $LaMnO_3$ is an A-type anti-ferromagnetic insulator [9]. When $LaMnO_3$ is doped with Sr, a rich phase diagram is observed, where the metallicity and the magnetic state changes as a function of the Sr fraction [11]. For instance, $La_{0.7}Sr_{0.3}MnO_3$ has a ferromagnetic ground state. Since Sr carries a formal charge of 2+, the Jahn-Teller distortions become weaker in the doped material [12]. The crystal structure of $La_{0.7}Sr_{0.3}MnO_3$ is rhombohedral [12]. Doping can affect the surface composition strongly since in Sr doped $LaMnO_3$, the surface is Sr enriched compared to the bulk [13]. Sr segregation was explained by surface polarization [14] and size effects [15].

As is typical for partially occupied d-orbitals, the electronic structure of Mn^{3+} is difficult to describe for standard DFT methods [16]. Hybrid DFT methods are an expensive alternative that result in better electronic properties [17]. Although, for the HSE functional a universal value for the mixing parameter predicting both band gap and magnetic exchanges interactions in $LaMnO_3$ accurately was not found [18]. Identification of a universal value for U is also a difficulty when applying the cost effective DFT+U method. While a value of U=4eV was determined to give good formation energies for manganese oxides [19, 16], at that value of U, the PBE+U method predicted the ferromagnetic state to be the ground state of $LaMnO_3$. In contrast, the correct A-type anti-ferromagnetic ground state was obtained with the PBE and PW91 functionals [18, 20]. As the U value increases, the difference between the ferromagnetic and anti-ferromagnetic states decreases, which was

accounted for by the destabilization of the ferromagnetic state due to strong orbital ordering [21]. Furthermore, the performance of the PBE+U method worsens when instead of experimental structures optimized geometries are used [21]. Regardless, standard DFT and DFT+U methods are most commonly used for the investigation of $LaMnO_3$ and Sr doped $LaMnO_3$.

The (001) surfaces of $LaMnO_3$ and Sr doped $LaMnO_3$ were often computationally studied in the context of solid oxide fuel cells with high operating temperatures, where the cubic phase is stable [22, 23, 24, 25, 26]. Oxygen interactions with the surface were of particular interest [27, 28, 29, 30, 31] since oxygen is electrochemically reduced at the cathode. In addition, hydroxylation of the $LaMnO_3$ surface and its implication for wetting and the oxygen reduction reaction were investigated [32]. This relates to our work of methanol/methoxy interactions with the surface. Similarly to water and hydroxyls [32] that have a higher affinity to the LaO than to the MnO_2 termination of (001) $LaMnO_3$, we will show that the adsorption energy of methanol is larger on the LaO than on the MnO_2 termination but, depending on Sr dopant amount and distribution, the adsorption energy ratio can be reversed.

2. Computational Details

All electronic structure calculations are carried out using the projector-augmented wave (PAW) method [33, 34] as implemented in the Vienna ab initio simulation package (VASP) [35, 36, 37, 38]. For surface and adsorbate calculations, we employ spin-polarized functionals [39, 40], an energy cut off of 400 eV, and a Γ-centered 4-4-1 Monkhorst-Pack k-point mesh. Dispersion

corrections are included through the D3 method by Grimme [41].

In order to choose a functional form, we perform bulk calculations for $LaMnO_3$ using selected functionals. In previous work [21], the PBE+U [39, 42] method with U = 2 eV gave the correct A-type anti-ferromagnetic ground state for the fully optimized $LaMnO_3$ geometry (although using a different program package, QMAS), while a value of 4 eV for U [19, 16] and the revised PBE (revPBE) [39, 40] functional predicted formation energies for manganese oxides well [43]. Using the experimental structure [10] at room temperature described within the Pbnm space group (Exp in Table 1), we calculated electronic properties of $LaMnO_3$ with the PBE+U for U=2,3,4 eV and with the revPBE functionals. For the A-type anti-ferromagnetic state, the indirect band gaps and average magnetic moments at Mn sites are given in Table 1. The band gaps are similar to the ones previously reported [18] for PBE and PBE+U for a slightly different geometry. As expected [18] and compared to experimental results (1.0-2.0 eV) [44, 45, 46], the revPBE method underestimates the band gap. The U parameter directly manipulates the band gap, which increases towards the experimental values with increasing U. Formally, the electronic configuration in Mn^{3+} is 3 t_g, 1 e_g, which results in an ideal magnetic moment of 4 μ_B. The computed magnetic moments do not change much with the computational method employed and compare well with the measured magnetic moment of 3.7 μ_B [9]. Also included in Table 1 are magnetic coupling constants (J_c). J_c measures the energetic difference between the ferromagnetic (E_{FM}) and the A-type anti-ferromagnetic state (E_{AAF}) and, applying a classical Heisenberg Hamiltonian

[18], is given by

$$E_{FM} - E_{AAF} = -32J_c \quad (1)$$

Our values follow the previously observed trend [18] that as U increases, so does J_c. Absolute values depend on subtle differences in the computational set up and the experimental structure used. Predicting small energy differences in the magnetic states (smaller than 0.03 eV) is indeed a difficult task for DFT. The validity of the Heisenberg picture should also be critically assessed [18] when comparing the experimental value of $J_c = -1.16$meV [18, 47] to computational results. However, the magnetic order is predicted correctly (negative J_c) for the experimental structure with revPBE while the use of U increases J_c to where, at U=3, 4 eV, reverse magnetic order is computed. Although, hybrid functionals perform reasonably for the band gap and J_c [18], they are too costly for our application. Despite the underestimation of the band gap with revPBE and in line with others [48], we prefer not to use the +U method but regard correct magnetic ordering and the reproduction of formation energies [43] as more desirable properties of the revPBE functional.

Further, we explore how J_c changes for the optimized structures (Opt in Table 1). To compute optimized bulk structures we perform constant volume calculations, where the cell shape is allowed to change. The optimized volume is obtained by a fit to the Murnaghan equation of state. Lattice constants and atomic positions are calculated for the optimized volume and for the desired magnetic state. We observe (see Table 1) that the ferromagnetic state is wrongly predicted to be more stable than the anti-ferromagnetic state for all tested methods. There is no clear trend as to the effect of U. Included in

Table 1: Indirect band gap for the A-type anti-ferromagnetic state in eV, average total magnetic moments μ at Mn sites in μ_B, magnetic coupling constant J_c (see text) in meV for the experimental structure at room temperature [10] (Exp) and optimized geometries (Opt) using different functionals; also included are r-ratios describing the extent of Jahn-Teller distortion (see text) for the ferromagnetic (FM) and A-type anti-ferromagnetic (AAF) states.

functional	Exp			Opt		
	Gap	μ	J_c	J_c	r (FM)	r (AAF)
revPBE	0.26	3.5	-0.60	3.73	0.97	0.89
PBE+U, U=2eV	0.71	3.7	-0.15	1.86	0.96	0.88
PBE+U, U=3eV	0.92	3.8	0.38	1.18	0.90	0.88
PBE+U, U=4eV	1.09	3.8	0.92	1.61	0.89	0.88

Table 1 is the ratio r for the ferromagnetic and the anti-ferromagnetic state. This is a measure of the Jahn-Teller distortions experienced in the material. These distortions elongate two Mn-O distances along one direction, leaving four Mn-O distances at shorter and similar values. The ratio, r, shown in Table 1 is the ratio between shortest and longest Mn-O distance and is 0.88 in the experimental structure. An important point to realize is that r remains close to the experimental structure in the optimized anti-ferromagnetic state but varies as a function of U in the optimized ferromagnetic state, thereby, influencing the relative energies of the states. Since Jahn-Teller distortions are well predicted for A-type anti-ferromagnetic $LaMnO_3$ and the magnetic ordering is calculated correctly for the experimental structure when using revPBE, we believe that the error in J_c calculated with revPBE for the optimized geometries stems from an errouneous structure prediction of the

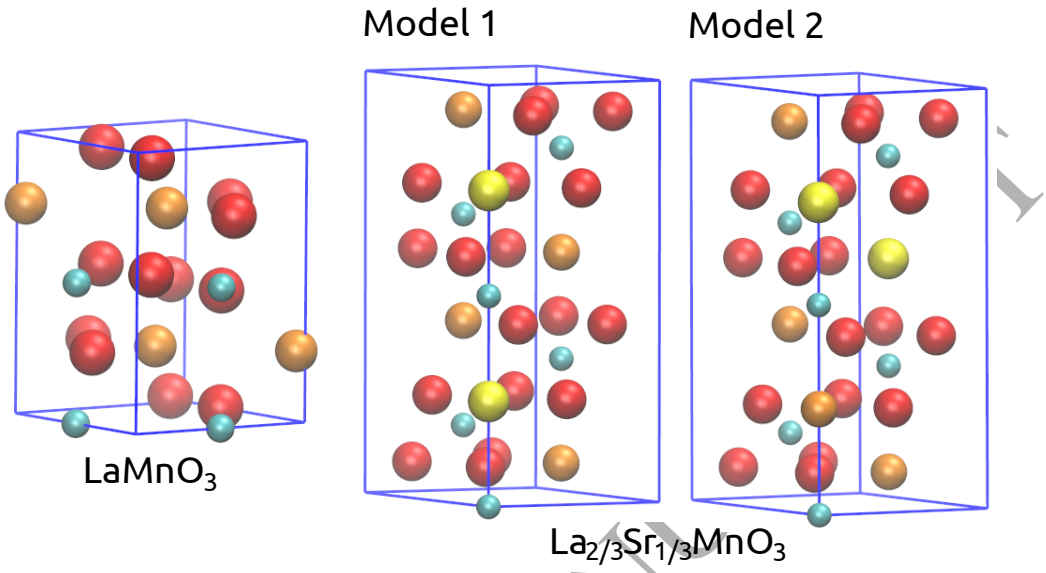

Figure 1: Unit cells of bulk $LaMnO_3$ and $La_{2/3}Sr_{1/3}MnO_3$ (model 1 and 2), atoms are rendered using scaled (by 0.5) crystal ionic radii [49], red - oxygen, cyan - manganese, orange - lanthanum, yellow - strontium.

ferromagnetic state. We, therefore, retain our choice and use the revPBE functional to describe the A-type anti-ferromagnetic state of $LaMnO_3$ and for all calculations that are described in the remainder of this text. In addition, this work is mainly concerned with the computation of adsorption energies, where errors due to the overstabilization of magnetic states are expected to at least partially cancel. Still, for Sr doped $LaMnO_3$, the overstabilization of the optimized ferromagnetic state is concerning since the magnetic state changes as a function of doping level. The exploration of this issue is, however, beyond the scope of this work.

The computed lattice parameters for bulk A-type anti-ferromagnetic $LaMnO_3$ are a = 5.576 Å, b = 5.834 Å, and c = 7.720 Å, compared to the experi-

mental lattice constants of a = 5.537 Å, b = 5.747 Å, and c = 7.693 Åat room temperature [10]. The orthorhombic unit cell is shown in Figure 1. To model the Sr doped bulk material we start with the experimental structure of $La_{0.7}Sr_{0.3}MnO_3$ [12] at 15 K. In the experimental structure the La versus Sr positions are not resolved. We take the hexagonal unit cell and replace two La atoms by Sr for a composition of $La_{2/3}Sr_{1/3}MnO_3$. In order to model different Sr distributions in the surface cells, we optimize two bulk models. In model 1, the Sr atoms are at a distance of 5.56 Å, and in model 2, the Sr atoms are separated by 3.85 Å. The hexagonal unit cells of both models are depicted in Figure 1. The optimized lattice constants for the ferromagnetic state of model 1 are a = 5.563 Å, c = 13.465 Åand of model 2 a = 5.563 Å, c = 13.425 Åcompared to the experimental lattice constants for $La_{0.7}Sr_{0.3}MnO_3$ [12] of a = 5.502 Å, c = 13.341 Å. Model 2 has a slightly lower energy (by 0.03 eV) than model 1.

The (001) surface of orthorhombic $LaMnO_3$ is constructed by stacking 8 atomic layers that extend periodically in the x- and y-directions. The equivalent plane in the hexagonal cell of the doped material is the $(11\bar{2}4)$ plane. However, for simplicity and for consistency with literature [30, 50], we use the term (001) surface for doped $LaMnO_3$ as well. Although the presence of oxygen vacancies can influence absorption properties and is more likely to occur in doped $LaMnO_3$ (with a vacancy formation on the order of 3eV [31]), in this work, we restrict ourselves to the stoichiometric materials. We employ a stoichiometric slab that contains an even number of alternating LaO (SrO or $LaSrO_2$ for doped $LaMnO_3$) and MnO_2 layers and is terminated on one side by a LaO (SrO, $LaSrO_2$) and on the other side by a MnO_2 layer. The

relaxed surface is obtained by optimization of the top six layers with desired surface termination while keeping the bottom two layers fixed simulating the bulk. The stoichiometric slab has a dipole moment normal to the surface for which dipole corrections are applied. Note that reconstruction of the polar surface may occur but is not considered in this work and other [20, 22, 23, 24, 25, 28, 29, 32, 48]. The dipole correction calculated by VASP for the MnO_2 terminated $LaMnO_3$ stoichiometric slab is an order of magnitude larger (0.10 eV) than for the nine-layered non-stoichiometric slab (0.02 eV). The dipole moment can be avoided by using a non-stoichiometric slab [28, 29]. Surface energies are similar for the two slabs [23]. However, in the non-stoichiometric slab, the oxidation state of the metals is altered, which affects oxygen vacancy formation energies [23] and may, likewise, influence the redox chemistry on the surface (which we will investigate in future work). We, therefore, employ the stoichiometric slab. Similarly to previous work [23], we find that the MnO_2-terminated eight-layered stoichiometric slab is not quite converged (0.06 J/m^2 difference in surface energy between eight and twelve-layered slabs). However, the surface energy of a 16-layer MnO_2-terminated stoichiometric slab with six relaxed top layers is converged with respect to the number of relaxed layers (below 0.002 J/m^2) and we anticipate that any effect due to the neglect of additional bulk layers cancels for the calculation of adsorption energies as is the main goal of this work. A vacuum layer of 15 Åis added in the z-direction to avoid interactions between slabs.

To investigate adsorbate-surface interactions, we use a p(1x1) expansion of the surface cell that contains one (dissociatively) adsorbed methanol. This corresponds to a coverage of methanol on the $LaMnO_3$ surface of 3.1 nm^{-2}

with slight deviations ($\leq 0.2\text{nm}^{-2}$) for the doped material and simulates a fairly high coverage that is typical for initial conditions in a TPD experiment [3]. During optimizations of minimum adsorbate structures and reaction paths, the top six atomic layers are relaxed while the remaining two layers are fixed. Minimum energy paths are optimized with the climbing image nudged elastic band method [51] (CI-NEB), where we use tools provided by the Henkelman group to set up the input. Transition states are confirmed by frequency analysis. A positive adsorption energy indicates exothermic adsorption. The dissociative adsorption energy is defined as the sum of adsorption energy and dissociation energy. For the case of methanol, it is the difference between the energy of methoxy and coadsorbed hydrogen on the surface and the sum of the energy of methanol and the energy of the surface. Bader charge analysis was carried out with the code provided by the Henkelman group [52, 53, 54].

3. Results and Discussion

3.1. Surfaces

The optimized bulk geometries shown in Figure 1 are used to build six surface models of the (001) surface, for the MnO_2 and the LaO ($LaSrO_2$, SrO) termination of each bulk model. Although, it was argued [25, 48] that the MnO_2 termination is more stable than the LaO termination, we are interested in the adsorption strength of methanol on both. This is because adsorbates [30] and Sr dorping [25] change the stability of the surface termination. In addition, in a realistic catalyst both surface terminations may be present. For doped $LaMnO_3$, we cleave bulk model 1 such that one Sr atom is on

the surface or subsurface for the $SrLaO_2$ or MnO_2 termination, respectively, while the other Sr atom is located four layers below that. Bulk model 2 is cleaved such that the surface and subsurface layer contains only Sr and O atoms for the SrO and the MnO_2 termination, respectively. Four an eight-layered p(1x1) expansion of the surface cell, the composition of the doped surface is then $Sr_{1/4}La_{3/4}MnO_2$. Model 1 and model 2 simulate different degrees of Sr enrichment in the surface [13].

Because of the size mismatch between the La and O atoms, the MnO_6 octahedra in $LaMnO_3$ are tilted. This tilt is maintained in the doped material. When the bulk is cleaved to yield the MnO_2-terminated surface, the octahedra are cut and the oxygen atoms on the surface have different positions along the z-axis due to the tilt. In response to cleavage, the octahedra reorient to allow the surface oxygen atoms to be in the surface plane. The reorientation of the MnO_6 octahedra on the MnO_2-terminated surface was observed for $LaMnO_3$ as well as doped models 1 and 2. When the bulk is cleaved to yield the LaO- ($SrLaO_2$-, SrO-) terminated surface, the MnO_6 octahedra remain intact and the octahedral tilt at the surface is preserved in the relaxed structure. The side view of the cleaved bulk and the relaxed surfaces can be found in the Supporting Information, Figure S1. This view also shows that in response to surface cleavage, the distance between surface and subsurface layer increases for both terminations of the $LaMnO_3$ surface and surface model 1. However, when all La atoms are replaced by Sr in the surface or subsurface layer in model 2, this distance decreases instead. The change in surface-subsurface distance causes a response in the separation between subsequent layers. Similarly, octahedral tilting angles and bond

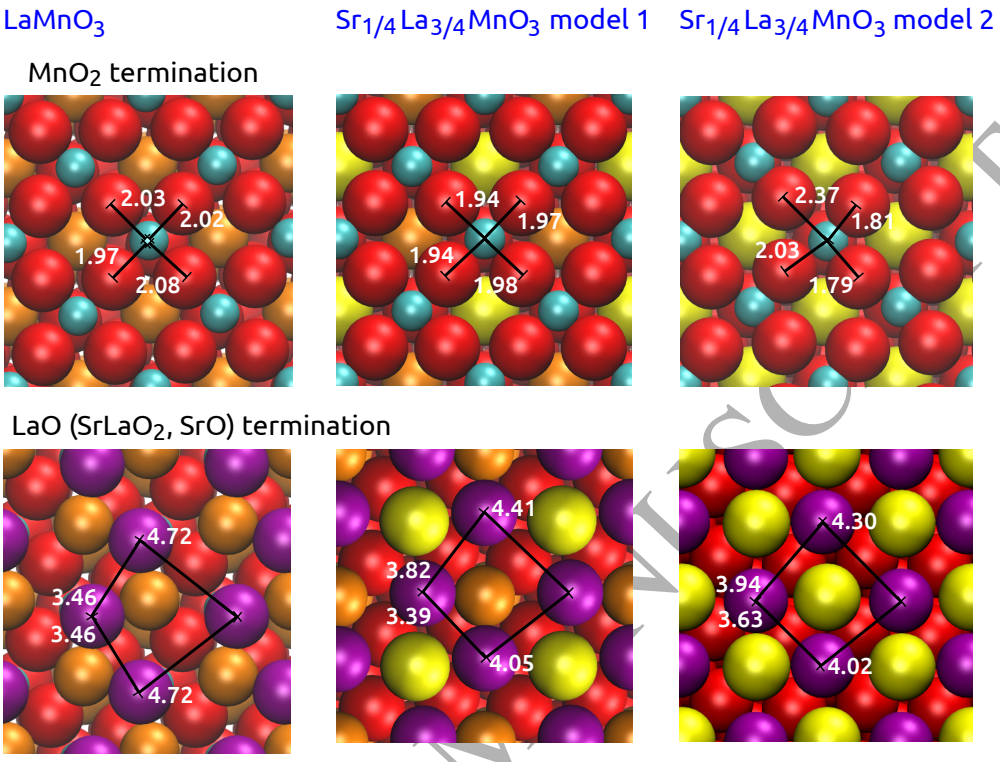

Figure 2: Surface top views; atoms are rendered using crystal ionic radii [49], red - oxygen, purple - oxygen in top layer of LaO-, $SrLaO_2$-, SrO-terminated surface, cyan - manganese, orange - lanthanum, yellow - strontium; distances in Å.

changes within the layers adjust from surface to bulk values within the top six layers that are allowed to relax in our calculations. The surface triggered distortions into the bulk are most likely not converged for the eight-layered slab [50] despite the convergence in surface energy with respect to the number of relaxed layers (see computational details).

Figure 2 shows the top view of the relaxed surfaces, the top view of the cleaved bulk can be found in the Supporting Information, Figure S2. In the cleaved bulk structure of the MnO_2-terminated $LaMnO_3$ surface, the

Jahn-Teller distortion is visible in the top layer; the Mn-O distances are 0.25 Ålonger in one direction of the MnO_6 octahedra compared to the other. As the surfaces relaxes, the Mn-O distances in the top layer become similar. Jahn-Teller distortions in the doped material are expected to be diminished [12] and are not apparent in the doped bulk structures that we calculated, see Supporting Information, Figure S2. Although for the ferromagnetic state, the degree of distortion is a function of the method used, see computational details. We observe an interesting difference between the surface response of doped model 1 and 2 for the MnO_2-terminated surface. While the Mn-O distances in the surface layer remain similar, although shorter than in $LaMnO_3$, when the subsurface layer contains 50% La and 50% Sr (model 1), the Mn atom moves away from the octahedron center towards an octahedral edge within the surface plane when the subsurface layer contains 100% Sr (model 2). This causes two adjacent Mn-O distances to decrease and, in particular, one Mn-O distance to be more than 0.55 Ålonger compared to the shortened bonds. In contrast to the MnO_2-terminated surface, the LaO-terminated surface shows wide spacing between oxygen atoms of the top layer with an asymmetric distribution of O atoms that surround La [48] or Sr. The largest distance between oxygen atoms in the top layer decreases as the Sr content increases, due to the larger size of the Sr^{2+} ion (132 pm [49]) compared to the La^{3+} ion (117.2 pm [49]).

The MnO_2 and LaO layers in $LaMnO_3$ formally carry a charge of -1 e and +1 e per MnO_2 and LaO unit, respectively. Using Bader analysis we evaluate the sum of atomic charges of the top layer of the surface cell per MnO_2 and LaO ($(SrLaO_2)/2$, SrO) unit, respectively, and compare to the

Table 2: Sum of atomic Bader charges for the surface q_S [e] and corresponding bulk values q_b [e] for the top layer of the surface cell per MnO_2 and LaO ($(SrLaO_2)/2$, SrO) unit, respectively, differences Δq [e] between bulk and surface charges and contributions from O, Mn, La, and Sr atoms; MnO_2 and LaO ($SrLaO_2$, SrO) terminations of $LaMnO_3$ and Sr doped models 1 and 2.

	$LaMnO_3$	Model 1	Model 2
MnO_2 termination			
q_S	-0.80	-0.70	-0.46
q_b	-0.89	-0.75	-0.74
Δq	-0.08	-0.05	-0.28
Δq O	-0.13	-0.13	-0.31
Δq Mn	0.04	0.08	0.03
LaO ($SrLaO_2$, SrO) termination			
q_S	0.69	0.48	0.32
q_b	0.89	0.66	0.42
Δq	0.19	0.18	0.10
Δq O	0.11	0.11	0.07
Δq La/Sr	0.08	0.07	0.02

corresponding values in the bulk. The charges are given in Table 2. The bulk charge of -0.89 e for the MnO_2 layer is compensated by a charge of 0.89 e for the LaO layer in $LaMnO_3$. In the doped material, the absolute bulk values for the oppositely charged layers are not the same since they depend on the location of the Sr atoms. If the bulk is cleaved, a layer is exposed whose charge is only partially compensated on one side by an oppositely charged layer. This is schematically shown for the MnO_2 termination in Fig-

ure 3 with a corresponding scenario for the LaO termination. The response of the MnO_2 surface to cleavage in $LaMnO_3$ is to reduce the negative surface charge through electron donation from the surface oxygen into the bulk with some electrons from oxygen also being absorbed by Mn^{3+}. When Sr^{2+} replaces either one or two La^{3+} ions in the surface cell, the corresponding bulk charges of the neighbouring MnO_2 layer is slightly reduced. However, the remaining charge of -0.75 e in the surface layer experiences less compensating charge from the layer below, see Figure 3. While the surface response to cleavage of the MnO_2 layer in model 1, where 50% of La^{3+} is replaced in the subsurface, is similar to the response in $LaMnO_3$, we observe a much larger difference between surface and bulk charges when 100% of La^{3+} is replaced in the subsurface. In model 2, the negative surface charge is not compensated on either side by a positively charged layer. The surface charge reduction in response to cleavage in model 2 originates from the oxygen atoms with little charge absorption by Mn^{3+}. For the LaO-terminated surface, the top layer is charged positively and the surface response to cleavage in $LaMnO_3$ is for the O^{2-} and the La^{3+} ions to absorb charge from the bulk to reduce the surface charge. When Sr^{2+} replaces 50% of the top layer La^{3+} ions in model 1 and 100% of the La^{3+} ions in model 2, the corresponding bulk charge is increasingly reduced. While, as for the MnO_2 termination, the surface response to cleavage in model 1 is similar to the response in $LaMnO_3$, we observe a relatively small charge redistribution in model 2. For the LaO (SrLaO, SrO) termination, electron gain on O^{2-}, La^{3+}, and Sr^{2+} all contribute to the charge reduction of the surface layer.

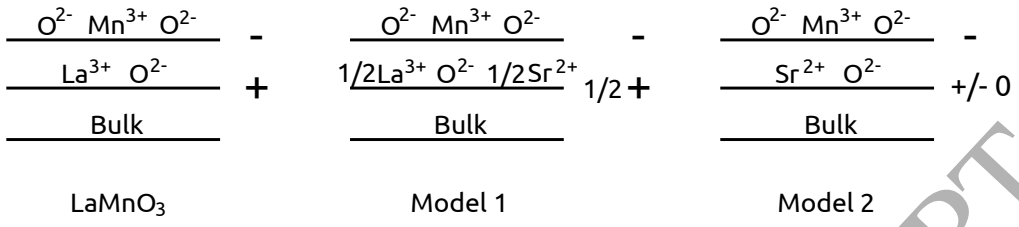

Figure 3: Schematic representation of surface charges on the MnO_2-terminated (001) surface of $LaMnO_3$ and Sr doped models 1 and 2.

3.2. Adsorbates

We probe the properties of the surfaces described in the previous section with methanol. Figure 4 shows the energetically lowest structures on the different surfaces for methanol adsorbed and methanol dissociatively adsorbed forming methoxy and hydrogen. Methanol and methoxy bind atop Mn on the MnO_2-terminated surfaces. On the LaO-terminated $LaMnO_3$ surface, methanol binds atop La. An energetically lower structure is obtained for doped model 1, when methanol binds atop Sr instead of La. For doped model 2, only Sr is available for atop binding on the surface. In contrast to the MnO_2-terminated surface, on the LaO- ($SrLaO_2$-, SrO-) terminated surface, methoxy prefers to bind in a bridge position between La, La/Sr, and Sr depending on dopant level at the surface. The activation energy for O-H cleavage in methanol on the MnO_2-terminated $LaMnO_3$ surface is 0.24 eV. The corresponding CI-NEB path is included in the Supporting Information, Figure S3. On the LaO-terminated $LaMnO_3$ surface, a bridge position for adsorbed molecular methanol could not be located. All optimization attempts led to dissociated methanol. Methanol approach onto the LaO-terminated $LaMnO_3$ surface forming dissociatively adsorbed methanol

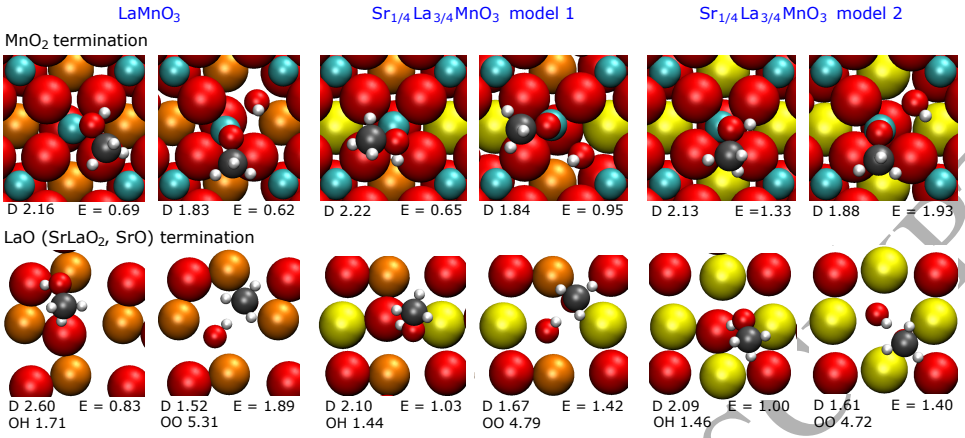

Figure 4: Energetically lowest structures for methanol adsorbed and methanol dissociatively adsorbed on the MnO_2- and LaO-($SrLaO_2$-, SrO-) terminated surfaces of $LaMnO_3$ and Sr doped models 1 and 2, top views; surface atoms are rendered using crystal ionic radii [49], atoms that possess covalent bonds are rendered using covalent radii [55]; top surface layer is show for LaO termination, top two layers for MnO_2 termination; red - oxygen, cyan - manganese, orange - lanthanum, yellow - strontium, gray - carbon, white - hydrogen; E - (dissociative) adsorption energies in eV; D - distance between methanol/methoxy and surface in Å(defined in text), OO - distance between methoxy and surface oxygen in between which methoxy is located in Å, OH - distance between hydroxy hydrogen of methanol and interacting surface oxygen in Å.

is barrier-less. The corresponding CI-NEB path is included in the Supporting Information, Figures S4. We hypothesize that the barriers for O-H cleavage do not qualitatively change with doping and believe that at elevated temperature (i.e., room temperature), methanol as well as dissociatively adsorbed methanol will be present in equilibrium distribution on all investigated surfaces.

Also included in Figure 4 are the adsorption energies for methanol and the dissociative adsorption energies (defined in the computational details) for

methoxy/H on the surfaces. Methanol dissociation is slightly endothermic (by 0.07 eV) on the MnO_2-terminated $LaMnO_3$ surface and exothermic on all other investigated surfaces. Methanol and methoxy/H bind stronger on the LaO-terminated than on the MnO_2-terminated $LaMnO_3$ surface. For dissociatively adsorbed methanol the adsorption energy difference between methoxy atop Mn on the MnO_2 termination and methoxy bridging two La ions on the LaO termination is 1.27 eV, which is substantial. For Sr doped model 1, where 50% of La are replaced by Sr in either the surface or the subsurface layer, adsorption is also stronger on the $SrLaO_2$ termination than on the MnO_2 termination but to a lesser extent than on the $LaMnO_3$ surface. For doped model 2, where all of La is replaced by Sr in either the surface or the subsurface layer, this relationship is reversed and methanol as well as methoxy/H are more strongly bound on the MnO_2-terminated surface.

We observe that adsorption energies on the MnO_2-terminated surface are similar for $LaMnO_3$ and for doped model 1, albeit the dissociative adsorption energy is larger for model 1. However, there is a significant increase in adsorption strength when methanol (by 0.64 eV) and methoxy/H (by 1.31 eV) adsorb on the MnO_2-terminated surface of model 2, where the subsurface layer contains Sr and O only. Added in Figure 4 are distances between methanol/methoxy and the surface. We define this distance as the difference between the z-coordinate of the methanol/methoxy oxygen and the z-coordinate of the metal ion it is bound to. For bridged species we use the average of the z-coordinates of the two involved metal ions. For the MnO_2-terminated surfaces, the distance between methanol and the surface is similar for $LaMnO_3$ and the Sr doped models. The distances be-

tween methoxy and the surface for dissociatively adsorbed methanol can also not be correlated with the adsorption energies. The hydroxy proton in methanol is separated by more than 2.1 Åto any surface oxygen indicating that the hydrogen/surface interaction is not a strong contribution to the adsorption strength. Instead, the interaction between methanol and the MnO_2-terminated surfaces is dominated by the interaction between an electron pair of the methanol oxygen and empty states of Mn. In dissociatively absorbed methanol, the negatively charged oxygen atom of methoxy interacts with the surface, although the hydrogen/surface interaction contributes as well. It is plausible that the reduction in negative surface charge observed for the doped surfaces (see previous section), particularly for model 2, facilitates interaction with the electron pair in methanol by decreasing electrostatic repulsion, even more so for the negatively charged methoxy. This is a possible explanation for the increased adsorption strength on the MnO_2-terminated surface of doped model 2.

In contrast to the MnO_2-terminated surfaces, methanol adsorption is aided by hydrogen/surface interactions on the LaO- ($SrLaO_2$-,SrO-) terminated surfaces. As depicted in Figure 4, the hydroxy group points towards the surface for a hydrogen/ surface oxygen distance of 1.71 Åin $LaMnO_3$, which becomes shorter in the Sr doped models. Also the distance between methanol and the surface is shorter for the doped models than in $LaMnO_3$. This is in line with a slightly increased adsorption energy for methanol binding atop Sr in the doped models compared to methanol bound atop La in $LaMnO_3$. The large dissociation energy for methanol on the LaO-terminated $LaMnO_3$ surface is accompanied by a considerable decrease (larger than on

the MnO_2 termination) in adsorbed species to surface distance, by 1.08 Å. As we have described in the previous section, the LaO termination of $LaMnO_3$ is characterized by wide spaces of 4.72 Åbetween oxygen atoms in the top layer. This gives the methoxy the opportunity for a closer approach to the surface when settling between these oxygen atoms. When methoxy adsorbs on the surface, the surface oxygen-oxygen distance is further increased to 5.31 Å(see Figure 4) indicating a flexible top layer with respect to atomic positions. As La is replaced by Sr in the surface layer, the surface oxygen-oxygen distances decrease due to the increased size of Sr^{2+} compared to La^{3+}. This decrease is fairly similar for models 1 and 2 with and without dissociatively adsorbed methanol (see Figure 4 and Figure 2) resulting in a similar decrease in dissociative adsorption energies for the doped models compared to LaO-terminated $LaMnO_3$.

4. Conclusion

Using DFT, we probed the MnO_2 and the LaO termination of the (001) surface of $LaMnO_3$ with methanol. We further investigated the influence of Sr doping on surface properties and (dissociative) adsorption energies of methanol. Since Sr is known to segregated towards the surface [13], we employed two different models of $Sr_{1/4}La_{3/4}MnO_2$. In model 1, 50% of La was replaced with Sr in the subsurface and surface layer for the MnO_2 and $SrLaO_2$ termination, respectively, with another layer of 50% La and 50% Sr four layers below. In model 2, 100% of La was replaced with Sr in the subsurface and surface layer, respectively. When $LaMnO_3$ and Sr doped $LaMnO_3$ are cleaved to yield the MnO_2-terminated surface, the MnO_6 octahedra, that

are tilted in the bulk are cut along the central plane exposing oxygen atoms with different positions relative to the surface plane. This causes a structural response, where the incomplete octahedra reorient to allow for a smooth surface. Cleavage to yield the LaO- ($SrLaO_2$-, SrO-) terminated surface leaves the MnO_6 octahedra intact and little restructuring is observed in response to cleavage. The LaO- ($SrLaO_2$-, SrO-) terminated surfaces are characterized by wide spaces in between the top layer oxygen atoms that allow the methoxy oxygen to settle in between the oxygen atoms in a bridged position between La, La/Sr, or Sr depending on doping level. Electron depletion in the surface layer compared to bulk values of the MnO_2-terminated surfaces and electron accumulation in the LaO- ($SrLaO_2$-, SrO-) terminated surfaces were explained as a function of dopant fraction in the surface or subsequent layer. Methanol is more strongly bound, both associatively and dissociatively, on the LaO- than on the MnO_2-terminated $LaMnO_3$ (001) surface. Activation energies for O-H cleavage in methanol on the surface are either small (0.24 eV) or barrier-less. The introduction of Sr decreases the dissociative adsorption energy of methanol on the LaO-terminated surface. While 50% of La replacement by Sr in the subsurface of the MnO_2 termination has little effect on the (dissociative) adsorption energies of methanol, when 100% of La is replaced by Sr, there is a significant increase in (dissociative) adsorption energy. This causes a reversal of the relative adsorption energy, adsorption is energetically favoured on the MnO_2 termination of the highly Sr enriched surface.

We hope that this study is a first step into understanding pathway selectivity during methanol conversion over $LaMnO_3$ and Sr doped $LaMnO_3$.

While both, the MnO_2 and the LaO (SrO) termination may be present under reaction conditions, catalytic conversion only occurs when methanol is bound to the surface; i.e., below the desorption temperature. Over $LaMnO_3$ methanol is available at the LaO terminated surface up to considerably higher temperature than on the MnO_2 terminated surface. If conversion over the MnO_2 termination is desired, a possible route is through Sr doping, where adsorption strength over the MnO_2 termination is increased in regions with high Sr enrichment in the surface.

Acknowledgements

This research is sponsored by the U.S. Department of Energy, Office of Science, Office of Basic Energy Sciences, Chemical Sciences, Geosciences, and Biosciences Division under contract number DE-AC05-00OR22725. This research was supported by an allocation of advanced computing resources provided by the National Science Foundation and performed on Darter and Beacon at the National Institute for Computational Sciences (http://www.nics.tennessee.edu/).

Supporting Information Available: Supporting information contains side view of the cleaved bulk and the relaxed surfaces, top view of the cleaved bulk, CI-NEB path for O-H cleavage in methanol on the MnO_2-terminated $LaMnO_3$ (001) surface, CI-NEB path for O-H cleavage in methanol on the LaO-terminated $LaMnO_3$ (001) surface. This material is available free of charge via the Internet at `http://www.sciencedirect.com`.

References

[1] Ramirez, A. P. Colossal Magnetoresistance. *J. Phys.: Condens. Matter* **1997**, *9*, 8171 – 8199.

[2] Kendall, K.; Kendall, M. *High-temperature Solid Oxide Fuel Cells for the 21st Century: Fundamentals, Design and Applications*; Elsevier, 2016.

[3] Mullins, D. R.; Albrecht, P. M.; Calaza, F. C. Variations in Reactivity on Different Crystallographic Orientations of Cerium Oxide. *Top. Catal.* **2013**, *56*, 1345 – 1362.

[4] Wu, Z. L.; Li, M. J.; Mullins, D. R.; Overbury, S. H. Probing the Surface Sites of CeO_2 Nanocrystals with Well-Defined Surface Planes via Methanol Adsorption and Desorption. *ACS Catalysis* **2012**, *2*, 2224 – 2234.

[5] Beste, A.; Overbury, S. H. Dehydrogenation of Methanol to Formaldehyde Catalyzed by Pristine and Defective Ceria Surfaces. *Phys. Chem. Chem. Phys.* **2016**, *18*, 9990 – 9998.

[6] Goldschmidt, V. M. Die Gesetze der Krystallochemie. *Die Naturwissenschaften* **1926**, *14*, 477 – 485.

[7] Peña, M. A.; Fierro, J. L. G. Chemical Structures and Performance of Perovskite Oxides. *Chem. Rev.* **2001**, *101*, 1981 – 2017.

[8] Tolerance Factor Calculator (2017, May 31) Retrieved from http://www.me.utexas.edu/∼benedekgroup/ToleranceFactorCalculator/#home.

[9] Elemans, J. B. A. A.; Van Laar, B.; Van Der Veen, K. R.; Loopstra, B. O. The Crystallographic and Magnetic Structures of $La_{1-x}Ba_xMn_{1-x}Me_xO_3$ (Me=Mn or Ti). *J. Solid State Chem.* **1971**, *3*, 238 – 242.

[10] Rodríguez-Carvajal, J.; Hennion, M.; Moussa, F.; Moudden, A. H. Neutron-Diffraction Study of the Jahn-Teller Trasition in Stoichiometric $LaMnO_3$. *Phys. Rev. B* **1998**, *57*, R3189 – R3192.

[11] Kozlenko, D. P.; Goncharenko, I. N.; Savenko, B. N.; Voronin, V. I. High Pressure Effects on the Crystal and Magnetic Structure of $La_{0.7}Sr_{0.3}MnO_3$. *J. Phys.: Condens. Matter* **2004**, *16*, 6755 – 6762.

[12] Hibble, S. J.; Cooper, S. P.; Hannon, A. C.; Fawcett, I. D.; Greenblatt, M. Local Distortions in the Colossal Magnetoresistive Manganates $La_{0.7}Ca_{0.3}MnO_3$, $La_{0.8}Ca_{0.2}MnO_3$ and $La_{0.7}Sr_{0.3}MnO_3$ Revealed by Total Neutron Diffraction. *J. Phys.: Condens. Matter* **1999**, *11*, 9221 – 9238.

[13] Fister, T. T.; Fong, D. D.; Eastman, J. A.; Baldo, P. M.; Highland, M. J.; Fuoss, P. H.; Balasubramaniam, K. R.; Meador, J. C.; Salvador, P. A. In Situ Characterization of Strontium Surface Segregation in Epitaxial $La_{0.7}Sr_{0.3}MnO_3$ Thin Films as a Function of Oxygen Partial Pressure. *Appl. Phys. Lett.* **2008**, *93*, 151904–1 – 151904–3.

[14] Harrison, W. A. Origin of Sr Segregation at $La_{1-x}Sr_xMnO_3$ Surfaces. *Phys. Rev. B* **2011**, *83*, 155437–1 – 155437–5.

[15] Lee, W.; Han, J. W.; Chen, Y.; Cai, Z.; Yildiz, B. Cation Size Mismatch

and Charge Interactions Drive Dopant Segregation at the Surfaces of Manganite Perovskites. *J. Am. Chem. Soc.* **2013**, *135*, 7909 – 7925.

[16] Franchini, G.; Podloucky, R.; Paier, J.; Marsman, M.; Kresse, G. Ground-State Properties of Multivalent Manganese Oxides: Density Functional and Hybrid Density Functional Calculations. *Phys. Rev. B* **2007**, *75*, 195128–1 – 195128–11.

[17] Muñoz, D.; Harrison, N. M.; Illas, F. Electronic and Magnetic Structure of $LaMnO_3$ from Hybrid Periodic Density-Functional Theory. *Phys. Rev. B* **2004**, *69*, 085115–1 – 085115–9.

[18] Franchini, C.; Kováčik, R.; Marsman, M.; Murthy, S. S.; He, J.; Ederer, C.; Kresse, G. Maximally Localized Wannier Functions in $LaMnO_3$ within PBE+U, Hybrid Functionals and Partially Self-Consistent GW: An Efficient Route to Construct Ab Initio Tight-Binding Parameters. *J. Phys.: Condens. Matter* **2012**, *24*, 235602–1 – 235602–17.

[19] Wang, L.; Maxisch, T.; Ceder, G. Oxidation Energies of Transition Metal Oxides within the GGA+U Framework. *Phys. Rev. B* **2006**, *73*, 195107–1 – 195107–6.

[20] Evarestov, R. A.; Kotomin, E. A.; Mastrikov, Y. A.; Gryaznov, D.; Heifets, E.; Maier, J. Comparative Density-Functional LCAO and Plane-Wave Calculations of $LaMnO_3$ Surfaces. *Phys. Rev. B* **2005**, *72*, 214411–1 – 214411–12.

[21] Hashimoto, T.; Ishibashi, S.; Terakura, K. Jahn-Teller Distortion and Magnetic Structure in $LaMnO_3$: A First-Principles Theoretical Study

with Full Structure Optimizations. *Phys. Rev. B* **2010**, *82*, 045124–1 – 045124–7.

[22] Kotomin, E. A.; Evarestov, R. A.; Mastrikov, Y. A.; Maier, J. DFT Plane-Wave Calculations of the Atomic and Electronic Structure of $LaMnO_3$ (001) Surface. *Phys. Chem. Chem. Phys.* **2005**, *7*, 2346 – 2350.

[23] Lee, Y.-L.; Kleis, J.; Rossmeisl, J.; Morgan, D. Ab Initio Energetics of $LaBO_3$(001) (B = Mn, Fe, Co, and Ni) for Solid Oxide Fuel Cell Cathodes. *Phys. Rev. B* **2009**, *80*, 224101–1 – 224101–20.

[24] Choi, Y.; Mebane, D. S.; Lin, M. C.; Liu, M. Oxygen Reduction on $LaMnO_3$-Based Cathode Materials in Solid Oxide Fuel Cells. *Chem. Mater.* **2007**, *19*, 1690 – 1699.

[25] Piskunov, S.; Heifets, E.; Jacob, T.; Kotomin, E. A.; Ellis, D. E.; Spohr, E. Electronic Structure and Thermodynamic Stability of $LaMnO_3$ and $La_{1-x}Sr_xMnO_3$ (001) Surfaces: Ab Initio Calculations. *Phys. Rev. B* **2008**, *78*, 121406–1 – 121406–4.

[26] Jalili, H.; Han, J. W.; Kuru, Y.; Cai, Z.; Yildiz, B. New Insights into the Strain Coupling to Surface Chemistry, Electronic Structure, and Reactivity of $La_{0.7}Sr_{0.3}MnO_3$. *J. Phys. Chem. Lett.* **2011**, *2*, 801 – 807.

[27] Pilania, G.; Gao, P.-X.; Ramprasad, R. Establishing the $LaMnO_3$ Surface Phase Diagram in an Oxygen Environment: An ab Initio Kinetic Monte Carlo Simulation Study. *J. Phys. Chem. C* **2012**, *116*, 26349 – 26357.

[28] Kotomin, E. A.; Mastrikov, Y. A.; Heifets, E.; Maier, J. Adsorption of Atomic and Molecular Oxygen on the $LaMnO_3$ (001) Surface: Ab initio Supercell Calculations and Thermodynamics. *Phys. Chem. Chem. Phys.* **2008**, *10*, 4644 – 4649.

[29] Pilania, G.; Ramprasad, R. Adsorption of Atomic Oxygen on Cubic $PbTiO_3$ and $LaMnO_3$ (001) Surfaces: A Density Functional Theory Study. *Surf. Sci.* **2010**, *604*, 1889 – 1893.

[30] Piskunov, S.; Jacob, T.; Spohr, E. Oxygen Adsorption at $La_{1-x}Sr_xMnO_3$(001) Surfaces: Predictions From First Principles. *Phys. Rev.* **2011**, *83*, 073402–1 – 073402–4.

[31] Chen, H.-T.; Raghunath, P.; Lin, M. C. Computational Investigation of O_2 Reduction and Diffusion on 25% Sr-Doped $LaMnO_3$ Cathodes in Solid Oxide Fuel Cells. *Langmuir* **2011**, *27*, 6787 – 6793.

[32] Stoerzinger, K. A.; Hong, W. T.; Azimi, G.; Giordano, L.; Lee, Y.-L.; Crumlin, E. J.; Biegalski, M. D.; Bluhm, H.; Varanasi, K. K.; Shao-Horn, Y. Reactivity of Perovskites with Water: Role of Hydroxylation in Wetting and Implications for Oxygen Electrocatalysis. *J. Phys. Chem. C* **2015**, *119*, 18504 – 18512.

[33] Blochl, P. E. Projector Augmented-Wave Method. *Phys. Rev. B* **1994**, *50*, 17953 – 17979.

[34] Kresse, G.; Joubert, D. From Utrasoft Pseudopotentials to the Projector Augmented-Wave Method. *Phys. Rev. B* **1999**, *59*, 1758 – 1775.

[35] Kresse, G.; Hafner, J. Ab Initio Molecular Dynamics for Liquid Metals. *Phys. Rev. B* **1993**, *47*, 558 – 561.

[36] Kresse, G.; Hafner, J. Ab Initio Molecular Dynamics Simulation of the Liquid-Metal-Amorphous-Semiconductor Transition in Germanium. *Phys. Rev. B* **1994**, *49*, 14251 – 14269.

[37] Kresse, G.; Furthmüller, J. Efficiency of Ab Initio Total Energy Calculations for Metals and Semiconductors Using a Plane-Wave Basis Set. *Comput. Mat. Sci.* **1996**, *6*, 15 – 50.

[38] Kresse, G.; Furthmüller, J. Efficient Iterative Schemes for Ab Initio Total Energy Calculations Using a Plane-Wave Basis Set. *Phys. Rev. B* **1996**, *54*, 11169 – 11186.

[39] Perdew, J. P.; Burke, K.; Ernzerhof, M. Generalized Gradient Approximation Made Simple. *Phys. Rev. Lett.* **1996**, *77*, 3865 – 3868.

[40] Zhang, Y.; Yang, W. Comment on "Generalized Gradient Approximation Made Simple". *Phys. Rev. Lett.* **1998**, *80*, 890.

[41] Grimme, S.; Antony, J.; Ehrlich, S.; Krieg, H. A Consistent and Accurate ab initio Parametrization of Density Functional Dispersion Correction (DFT-D) for the 94 Elements H-Pu. *J. Chem. Phys.* **2010**, *132*, 154104–1 – 154104–19.

[42] Dudarev, S. L.; Botton, G. A.; Savrasov, S. Y.; Humphreys, C. J.; Sutton, A. P. Electron-Energy-Loss Spectra and the Structural Stability of Nickel Oxide: An LSDA+U sudy. *Phys. Rev. B* **1998**, *57*, 1505 – 1509.

[43] Martínez, J. I.; Hansen, H. A.; Rossmeisl, J.; Nørskov, J. K. Formation Energies of Rutile Metal Dioxides Using Density Functional Theory. *Phys. Rev. B* **2009**, *79*, 045120–1 – 045120–5.

[44] Arima, T.; Tokura, Y.; Torrance, J. B. Variation of Optical Gaps in Perovskite-Type 3D Transition-Metal Oxides. *Phys. Rev. B* **1993**, *48*, 17006 – 17009.

[45] Tobe, K.; Kimura, T.; Okimoto, Y.; Tokura, Y. Anisotropic Optical Spectra In a Detwinned LaMnO3 Crystal. *Phys. Rev. B* **2001**, *64*, 184421.

[46] Kovaleva, N. N.; Boris, A. V.; Bernhard, C.; Kulakov, A.; Pimenov, A.; Balbashov, A. M.; Khaliullin, G.; Keimer, B. Spin-Controlled Mott-Hubbard Bands In LaMnO3 Probed by Optical Ellipsometry. *Phys. Rev. Lett.* **2004**, *93*, 147204.

[47] Moussa, F.; Hennion, M.; Rodriguez-Carvajal, J.; Moudden, H.; Pinsard, L.; Revcolevschi, A. Spin Waves in the Antiferromagnetic Perovskite $LaMnO_3$: A Neutron-Scattering Study. *Phys. Rev. B* **1996**, *54*, 15149.

[48] Hammami, R.; Batis, H.; Minot, C. Combined Experimental and Theoretical Investigation of the CO_2 Adsorption on $LaMnO_{3+y}$ Perovskite Oxide. *Surf. Sci.* **2009**, *603*, 3057 – 3067.

[49] Shannon, R. D. Revised Effective Ionic Radii and Systematic Studies of Interatomic Distances in Halides and Chalcogenides. *Acta Cryst* **1976**, *A32*, 751 767.

[50] Pruneda, J. M.; Ferrari, V.; Rurali, R.; Littlewood, P. B.; Spaldin, N. A.; Artacho, E. Ferrodistortive Instability at the (001) Surface of Half-Metallic Manganites. *Phys. Rev. Lett.* **2007**, *99*, 226101–1 – 226101–4.

[51] Henkelman, G.; Uberuaga, B. P.; Jónsson, H. A Climbing Image Nudged Elastic Band Method for Finding Saddle Points and Minimum Energy Paths. *J. Chem. Phys.* **2000**, *113*, 9901 – 9904.

[52] Tang, W.; Sanville, E.; Henkelman, G. A Grid-Based Bader Analysis Algorithm Without Lattice Bias. *Condens. Matter* **2009**, *21*, 084204–1 – 7.

[53] Sanville, E.; Kenny, S. D.; Smith, R.; Henkelman, G. An Improved Grid-Based Algorithm for Bader Charge Analysis. *J. Comp. Chem.* **2007**, *28*, 899 – 908.

[54] Henkelman, G.; Arnaldsson, A.; Jónsson, H. A Fast and Robust Algorithm for Bader Decomposition of Charge Density. *Comput. Mater. Sci.* **2006**, *36*, 254 – 360.

[55] Cordero, B.; Gómez, V.; Platero-Prats, A. E.; Revés, M; Echeverría, J.; Cremades, E.; Barragán, F.; Alvarez, S. Covalent Radii Revisited. *Dalton Trans.* **2008**, *21*, 2832 – 2838.

TOC